This document is downloaded from DR-NTU (https://dr.ntu.edu.sg)
Nanyang Technological University, Singapore.

Temperature effects on singlet fission dynamics mediated by a conical intersection

Sun, Kewei; Xu, Quan; Chen, Lipeng; Gelin, Maxim F.; Zhao, Yang

2020

Sun, K., Xu, Q., Chen, L., Gelin, M. F., & Zhao, Y. (2020). Temperature effects on singlet fission dynamics mediated by a conical intersection. The Journal of Chemical Physics, 153(19), 194106-. doi:10.1063/5.0031435

https://hdl.handle.net/10356/145943

https://doi.org/10.1063/5.0031435

© 2020 The Author(s). All rights reserved. This paper was published by AIP Publishing in The Journal of Chemical Physics and is made available with permission of The Author(s).

Downloaded on 09 Apr 2024 17:28:42 SGT

The Journal of Chemical Physics ARTICLE scitation.org/journal/jcp

Temperature effects on singlet fission dynamics mediated by a conical intersection

Cite as: J. Chem. Phys. 153, 194106 (2020); doi: 10.1063/5.0031435
Submitted: 30 September 2020 • Accepted: 30 October 2020 •
Published Online: 16 November 2020

Kewei Sun,[1] Quan Xu,[1,2] Lipeng Chen,[3] Maxim F. Gelin,[1,a)] and Yang Zhao[2,b)]

AFFILIATIONS

[1] School of Science, Hangzhou Dianzi University, Hangzhou 310018, China
[2] School of Materials Science and Engineering, Nanyang Technological University, Singapore 639798, Singapore
[3] Max-Planck-Institut für Physik komplexer Systeme, Nöthnitzer Strasse 38, D-01187 Dresden, Germany

Note: This paper is part of the JCP Special Topic on Excitons: Energetics and Spatio Temporal Dynamics.

[a)] **Electronic mail:** maxim@hdu.edu.cn
[b)] **Author to whom correspondence should be addressed:** YZhao@ntu.edu.sg

ABSTRACT

Finite-temperature dynamics of singlet fission in crystalline rubrene is investigated by utilizing the Dirac–Frenkel time-dependent variational method in combination with multiple Davydov D_2 trial states. To probe temperature effects on the singlet fission process mediated by a conical intersection, the variational method is extended to include number state propagation with thermally averaged Boltzmann distribution as initialization. This allows us to simulate two-dimensional electronic spectroscopic signals of two-mode and three-mode models of crystalline rubrene in the temperature range from 0 K to 300 K. It is demonstrated that an elevated temperature facilitates excitonic population transfer and accelerates the singlet fission process. In addition, increasing temperature leads to dramatic changes in two-dimensional spectra, thanks to temperature-dependent electronic dephasing and to an increased number of system eigenstates amenable to spectroscopic probing.

Published under license by AIP Publishing. https://doi.org/10.1063/5.0031435

I. INTRODUCTION

An exciton multiplication process, which allows an excited singlet state generated by irradiation to be converted to two triplet excitations in monomers as well as in the crystalline phase of organic molecular aggregates, singlet fission (SF) has attracted much attention as it can potentially enable photovoltaic devices to bypass the Shockley–Queisser limit in conversion efficiency.[1] Over the recent years, substantial progress has been achieved in scrutinizing SF mechanisms and pathways in pentacene/tetracene systems as well as in theoretical modeling of SF processes in a variety of contexts to engineer novel photovoltaic materials.[1–5]

It is nowadays well established that conical intersections (CIs) play a pivotal role in the SF process.[6–8] Furthermore, two mechanisms of CI-mediated SF have been established for crystalline rubrene.[5,7] The first one is the quantum coherent mechanism generated by the CI between the singlet S_1 state and the correlated triplet pair (TT) state. It was shown that a symmetry-breaking intermolecular mode triggers the interstate coupling in crystalline rubrene, opening up a new venue for engineering molecular systems with more efficient SF mechanisms. Spectroscopic manifestations of this mechanism at zero temperature have recently been studied by theoretical simulations in Ref. 9. The second one is the thermally assisted SF mechanism. It employs thermal activation for reaching the CI seam between the S_1 and TT states, where the interstate coupling is activated through the excitation of the symmetry-breaking modes. In addition, a pivotal role of vibrational modes in driving the SF process has been demonstrated.[8,10–12]

Nonlinear femtosecond spectroscopy is the main source of empirical knowledge on the SF dynamics. The corresponding experimental techniques include transient transmittance pump-probe spectroscopy,[6,7] time- and frequency-resolved fluorescence,[10,11] and two-dimensional (2D) electronic spectroscopy (2DES).[8,12] These techniques provide alternative views of the SF dynamics by projecting the multidimensional electronic/nuclear wave packets onto different electronic states.

To the best of our knowledge, little attention has been devoted so far to the accurate simulation of temperature effects on the

CI-mediated SF dynamics in organic molecular aggregates and its spectroscopic manifestations. These topics are the focus of the present work.

Spectroscopic signatures of CIs in the SF process have been analyzed so far in terms of phenomenological low-dimensional (reduced) CI models with several electronic states, a single vibrational coupling mode, and one or two vibrational tuning modes.[8,12] The numerically efficient and accurate hierarchy equation of motion (HEOM) method[13] has recently been applied to the simulation of electron–phonon dynamics[14–19] and nonlinear femtosecond spectroscopic signals[20–22] at CIs described by similar models. Therefore, combining the reduced models with the HEOM methodology could be feasible for the elucidation of the mechanistic role of CIs in the SF process at finite temperature. In the present work, however, we wish to develop the *ab initio*-based methodology, which permits the simulation of spectroscopic signals of the CI-driven SF systems on the basis of multidimensional potential-energy surfaces (PESs) constructed microscopically via quantum-chemical methods. The linear-vibronic-coupling (LVC) machinery in which PESs are represented by polynomials on nuclear coordinates is a reliable method for the construction of Hamiltonians of CI systems.[23] The wave-function-based methods, notably the (multilayer) multi-configuration time-dependent Hartree (MCTDH) method[24] and the variational multi-configurational Gaussian (vMCG) method,[25] are known to be highly efficient in modeling the CI dynamics driven by LVC Hamiltonians at zero temperature. However, the generalization of these methods to finite temperatures requires statistical sampling of initial conditions and is highly demanding computationally.[26–30] Hence, applications of the MCTDH to the simulation of spectroscopic signals at finite temperatures are quite limited.[31,32]

In the past decade, a method has been developed, which enables efficient, accurate simulation of optical responses of multimode systems with CIs through the evaluation of the third-order response functions within the framework of the Dirac–Frenkel time-dependent variation combined with a hierarchy of the multiple Davydov *Ansätze*.[9,33–36] On the one hand, this method performs well in grasping nonadiabatic dynamics at CIs. On the other hand, it is flexible and offers a good balance between the accuracy and efficiency by varying the multiplicity of the Davydov trial states. Yet, the Davydov *Ansatz* method for evaluating the third-order response functions was available only at zero temperature due to its construct of time-dependent variation. Werther *et al.* have recently proposed an approach that can be efficiently employed to introduce temperature effects into the Davydov trial states.[37,38] Two alternative approaches, the sampling of P-function method[39] and the thermo-field dynamics method,[40–42] are numerically demanding, which makes their application to the evaluation of third-order response functions somewhat time consuming.

In this work, we incorporate the method of Refs. 37 and 38 for the evaluation of the third-order response functions and investigate the thermally assisted SF mechanism in crystalline rubrene by accurate simulations of temperature effects in the CI-mediated SF population transfer and its spectroscopic signatures. The remainder of this paper is structured as follows: in Sec. II, we present the model Hamiltonian and introduce the methodology employed in this work. Simulations of the SF dynamics and 2DES signals are presented and discussed in Sec. III. The conclusions are drawn in Sec. IV.

II. METHODOLOGY

A. The CI model

Due to the complexity associated with the accurate simulation of the CI-driven SF at finite temperatures, we restrict ourselves to the consideration of two-electronic-state (S_1 and TT) and two/three-vibrational-mode models of SF in rubrene crystals. Here, S_1 is the (optically bright) singlet state and TT is the (optically dark) correlated triplet pair state. For simplicity, higher-lying singlet/triplet states and charge transfer states are not explicitly included in our simulation here. Yet, the present model gives valuable insight into the SF dynamics and its spectroscopic detection at finite temperatures as well as serves as a useful testing ground for the development of more realistic multidimensional and multistate microscopic models of the SF process in organic molecular aggregates.

In the diabatic representation, the system Hamiltonian H_S of the present model is represented as the sum of an electronic ground-state Hamiltonian H_g and an excited state Hamiltonian H_e,[9]

$$H_S = H_g + H_e. \tag{1}$$

Explicitly,

$$H_g = |g\rangle h_g \langle g|, \tag{2}$$

$$H_e = \sum_{k=S_1,TT} |k\rangle (h_k + \varepsilon_k)\langle k| + (|S_1\rangle\langle TT| + |TT\rangle\langle S_1|)\lambda Q_c. \tag{3}$$

Here, $|g\rangle$ denotes the electronic ground state, ε_{S_1} and $\varepsilon_{\mathrm{TT}}$ are the vertical excitation energies of the states $|S_1\rangle$ and $|\mathrm{TT}\rangle$, respectively, and λ is the interstate coupling constant responsible for the CI of $|S_1\rangle$ and $|\mathrm{TT}\rangle$. The vibrational Hamiltonians h_g, h_{S_1}, and h_{TT} include a single coupling mode (subscript c) as well as one (or two) primary tuning mode (subscript t),

$$h_g = \frac{1}{2}\sum_{\alpha=c,t} \Omega_\alpha (P_\alpha^2 + Q_\alpha^2), \tag{4}$$

$$h_k = h_g + \sum_{\alpha=t} \kappa_\alpha^k Q_\alpha. \tag{5}$$

Here, Ω_α, Q_α, and P_α are the frequencies, dimensionless coordinates, and dimensionless momenta of the modes, respectively, while κ_α^k are the linear intrastate electron-vibrational couplings. We have set $\hbar = 1$. The tuning modes Q_t are the dimensionless reaction coordinates of SF, while Q_c is an antisymmetric intermolecular coupling mode that couples the electronic states $|S_1\rangle$ and $|\mathrm{TT}\rangle$.

The LVC Hamiltonian of the CI model can also be recast in the operator form[9,36]

$$\begin{aligned}\hat{H}_S = {} & \sum_{k=S_1,TT} \epsilon_k |k\rangle\langle k| + \sum_{\alpha=t,c} w_\alpha \hat{b}_\alpha^\dagger \hat{b}_\alpha \\ & + \frac{\lambda}{\sqrt{2}}(|S_1\rangle\langle TT| + |TT\rangle\langle S_1|)(\hat{b}_c^\dagger + \hat{b}_c) \\ & + \frac{1}{\sqrt{2}}\sum_{\alpha=t}\sum_{k=S_1,TT} \kappa_\alpha^k |k\rangle\langle k|(\hat{b}_\alpha^\dagger + \hat{b}_\alpha),\end{aligned} \tag{6}$$

where $\hat{b}_\alpha^\dagger$ ($\hat{b}_\alpha$) is the electronic creation (annihilation) operator of the αth mode. This equivalent form of the Hamiltonian is convenient for the implementation of the Dirac–Frenkel variational principle.

The system, which contains all primary vibrational modes strongly affecting the SF process, is coupled to a harmonic phonon bath described by the Hamiltonian H_B, which mimics the impact of the remaining inter- and intramolecular modes on the SF dynamics,

$$H_B = \sum_{q}^{\mathrm{N_{bath}}} \hbar\Omega_q \hat{B}_q^\dagger \hat{B}_q. \tag{7}$$

The system-bath coupling Hamiltonian is assumed to be diagonal in the electronic space,

$$H_{SB} = \sum_{q=1}^{\mathrm{N_{bath}}} \sum_{k=S_1,TT} |k\rangle\langle k|\kappa_q^k(\hat{B}_q^\dagger + \hat{B}_q), \tag{8}$$

with κ_q^k being the system-bath coupling coefficients. To facilitate the interpretation of the obtained results, we assume that $\kappa_q^{S_1} = \kappa_q^{TT} = \kappa_q$. The so-defined bath does not affect electronic population relaxation ($[H_S, H_{SB}] = 0$) but induces the dephasing of coherences between the electronic states $|g\rangle$ and $|\mathrm{S}_1\rangle$, $|\mathrm{TT}\rangle$.[34,35] Then, the total third-order response functions describing spectroscopic signals of the SF system are expressed as products of the system and the bath response functions, where the bath response functions are evaluated analytically through the line shape functions of the Brownian oscillator model (see Appendix B).

B. Multiple Davydov *Ansätze* and physical observables

To treat Hamiltonians with off-diagonal coupling terms, Davydov D_2 trial states of multiplicity M, which essentially sum over M copies of the corresponding single-state Davydov D_2 *Ansatz*, are deployed to boost simulation accuracy. A generalized multi-D_2 *Ansatz* of multiplicity M for the displaced number state $|\vec{n}\rangle = |n_1 n_2 \cdots n_w\rangle$ used to include temperature effects reads[37,38]

$$\begin{aligned}|\psi_{\vec{n}}^M(t)\rangle =& |S_1\rangle \sum_{k=1}^{M} A_k^{\vec{n}}(t) e^{\left(\sum_q f_{kq}^{\vec{n}}(t) b_q^\dagger - H.c.\right)}|\vec{n}\rangle \\ &+ |TT\rangle \sum_{k=1}^{M} B_k^{\vec{n}}(t) e^{\left(\sum_q f_{kq}^{\vec{n}}(t) b_q^\dagger - H.c.\right)}|\vec{n}\rangle.\end{aligned} \tag{9}$$

Especially, for $\vec{n} = 0$, applying the displacement operator on the vacuum phonon state of the oscillator spawns a coherent state. Here, *H.c.* denotes the Hermitian conjugate. $A_k^{\vec{n}}(t)$ and $B_k^{\vec{n}}(t)$ denote, respectively, the time-dependent variational parameters for the amplitude in the diabatic states $|\mathrm{S}_1\rangle$ and $|\mathrm{TT}\rangle$. $f_{kq}^{n_q}(t)$ are the corresponding phonon displacements with the kth coherent state and the qth mode. The Eulerian equation of motion for time-dependent variational parameters $\vec{\mu} = \{A_k^{\vec{n}}(t), B_k^{\vec{n}}(t), f_{kq}^{n_q}(t)\}$ can be derived from the Dirac–Frenkel variational principle. Here, the Dirac–Frenkel Lagrangian is formulated as

$$\begin{aligned}L =& \frac{i}{2}\left[\langle\psi_{\vec{n}}^M(t)|\frac{\overrightarrow{\partial}}{\partial t}|\psi_{\vec{n}}^M(t)\rangle - \langle\psi_{\vec{n}}^M(t)|\frac{\overleftarrow{\partial}}{\partial t}|\psi_{\vec{n}}^M(t)\rangle\right] \\ &- \langle\psi_{\vec{n}}^M(t)|H|\psi_{\vec{n}}^M(t)\rangle.\end{aligned} \tag{10}$$

A detailed derivation of the equations that govern the time propagation of the variational parameters is given in Appendix A.

The time-dependent diabatic population of the electronic state $|\mathrm{S}_1\rangle$ for the number state $|n\rangle$ can be obtained by

$$P_{S_1}^{\vec{n}} = \sum_{m}^{M}\sum_{m'}^{M} A_m^{\vec{n}*}(t) A_{m'}^{\vec{n}}(t) S_{mm'}^{\vec{n}},$$

where the Debye–Waller factor is given by

$$S_{mm'}^{\vec{n}} = \exp\left(\sum_q\left\{-\left(\left|f_{mq}^{n_q}\right|^2 + \left|f_{m'q}^{n_q}\right|^2\right)/2 + f_{mq}^{n_q\,*} f_{m'q}^{n_q}\right\}\right). \tag{11}$$

Then, we adopt the Boltzmann-averaged method to calculate the observable from

$$P_{S_1}^{B} = \prod_l \sum_{n_l=0}^{N_{l,T}} \frac{e^{-\beta n_l \hbar\omega_l}}{Q_\beta} P_{S_1}^{\vec{n}},$$

where

$$Q_\beta = \prod_l \sum_{n_l=0}^{\infty} e^{-\beta n_l \hbar\omega_l} \tag{12}$$

is the canonical partition function and $\beta = 1/(k_B T)$ (k_B is the Boltzmann constant and T is the temperature). The truncated number of the lth phonon mode excitation $N_{l,T}$ yielding converged numerical results is determined by the temperature and the total phonon excitation energy.

It is well known that the number state $|n_l\rangle$ of the harmonic oscillator can be expanded in terms of coherent states,[43] which becomes

$$|n_l\rangle = \frac{1}{2\pi}\sqrt{\frac{n_l!\,e^{|\beta_l|^2}}{|\beta_l|^{2n_l}}}\int_{-\pi}^{\pi} d\theta_l e^{-in_l\theta_l}\,\||\beta_l|e^{i\theta_l}\rangle. \tag{13}$$

To discretize the integral over θ_l, we adopt the approximate expression

$$|n_l\rangle \approx \sqrt{\frac{n_l!\,e^{|\beta_l|^2}}{|\beta_l|^{2n_l}}}\frac{1}{N}\sum_{k_l=0}^{N-1} e^{-in_l\theta_{k_l}}\,\||\beta_l|e^{i\theta_{k_l}}\rangle, \tag{14}$$

where $\theta_{k_l} = -\pi + \frac{2\pi}{N}k_l$ and $k_l = 0, \ldots, N-1$.

Following the suggestion of Werther *et al.*,[37] for the Davydov-D$_2$ Ansatz with multiplicity $M \geq N^w$ (w is the number of modes that may be excited), the initial conditions with the w phonon modes read

$$A_k^{\vec{n}}(0) = \begin{cases}\prod_l \mathcal{N}(\beta_l)\exp(-in_l\theta_{k_l}), & 1 \leq k \leq N^w \\ 0, & else,\end{cases} \tag{15}$$

$$B_k^{\vec{n}}(0) = 0, \tag{16}$$

$$f_{kl}^{n_l}(0) = \begin{cases}|\beta_l|\exp(i\theta_{k_l}), & 1 \leq k \leq N^w \\ 0, & else,\end{cases} \tag{17}$$

TABLE I. Numerical values of the model parameters (in units of eV).

Energy	Mode	ω_l	$\kappa_l^{(1)}$	$\kappa_l^{(2)}$	λ_l
$E_{S1} = 2.23$	Ω_c	0.0154	0	0	0.0745
$E_{\mathrm{TT}} = 2.28$	Ω_{t1}	0.1860	0.3720	−0.3720	0
	Ω_{t2}	0.0260	0.0745	−0.0745	0

where $\mathcal{N}(\beta_l) = \frac{1}{N}\sqrt{\frac{(n_l!)e^{\beta_l^2}}{|\beta_l|^{2n_l}}}$. The convergence with respect to the number of sampling points N on the circle of radius $|\beta_l| = \sqrt{n_l}$ can be quickly obtained, for example, in Ref. 37, for N between 5 and 14 depending on various initial excitations n. In the subsequent simulations, we, thus, adopt $|\beta_l| = \sqrt{n_l}$, the value of best performance.[37]

In the present work, we monitor temperatures in the range from 0 K to 300 K (0 eV–0.0259 eV). The total phonon energy considered is, thus, within 0 eV–0.13 eV. The chosen maximal phonon energy, which is five times higher than the maximal thermal energy, ensures a high precision of samplings. Thus, the phonon excitation combinations can be directly given according to the total phonon excited energy for different models. We set $N = 14$ for the two-mode model and $N = 10$ for the three-mode model. For both models, a multiplicity of $M = 108$ is used in the simulations.

C. 2D spectroscopy

Two-dimensional electronic spectroscopy (2DES) is a femtosecond spectroscopic technique that allows the elucidation of system dynamics on the ultrafast timescale.[44,45] An optical analog of 2D infrared (IR) spectroscopy,[46] which is used to study vibrational excitations and transfer, 2DES probes atomic/molecular systems by a train of three mutually delayed ultrashort (tens of femtoseconds) laser pulses.

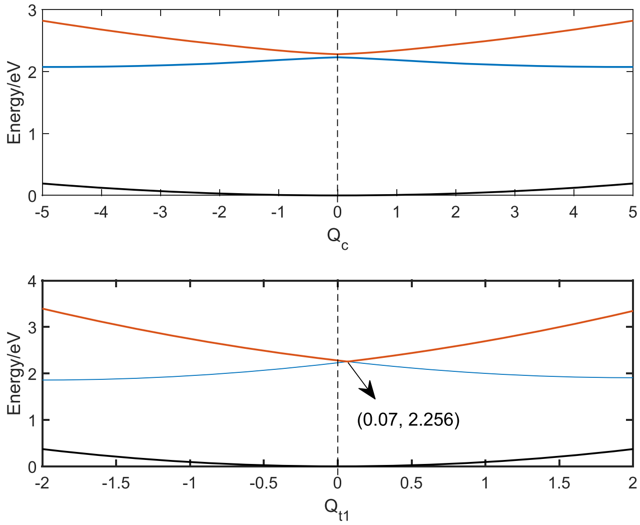

FIG. 1. Cuts through the adiabatic PESs of the S_1 (blue), S_{TT} (red), and *g* (black) states of the 2-mode model along the normal coordinates Q_c (upper panel) and Q_{t1} (lower panel).

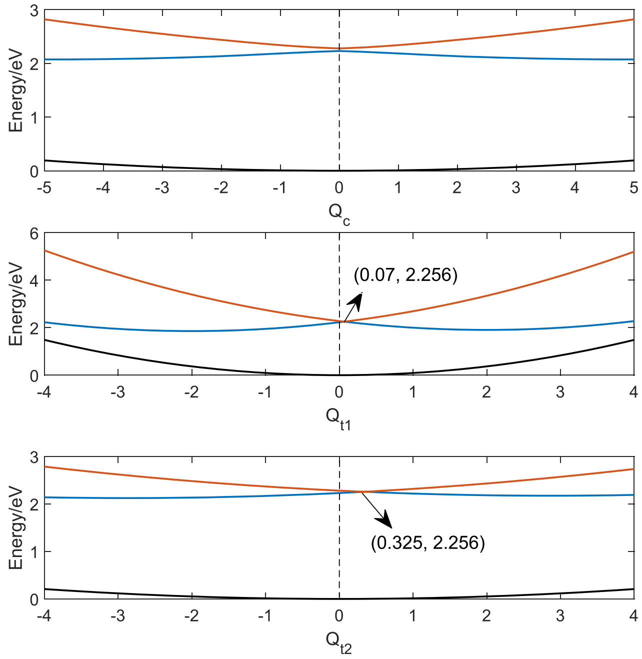

FIG. 2. Cuts through the adiabatic PESs of the S_1 (blue), S_{TT} (red), and *g* (black) states of the 3-mode model along the normal coordinates Q_c (upper panel), Q_{t1} (middle panel), and Q_{t2} (lower panel).

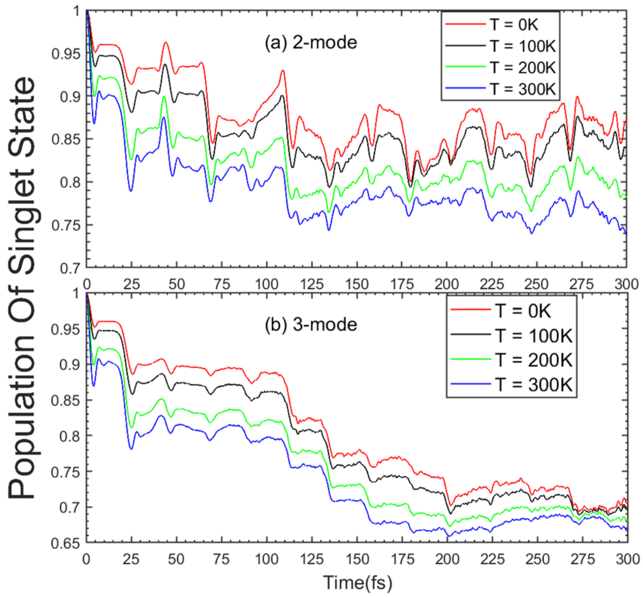

FIG. 3. Diabatic population dynamics of the singlet S_1 state for the (a) two- and (b) three-mode models for T = 0 K, 100 K, 200 K, 300 K.

If the pulses can be considered as short on the system dynamics timescale, the optical response of the system to the three pulses is fully described by the four third-order response functions $R_n(t_1, T_w, t_3)$, where n runs from 1 to 4. The delay between the first and second pulses is called the coherence time and is labeled as t_1. The delay between the second and third pulses is called the population time or the waiting time and is labeled as T_w. The time after the third pulse corresponds to the detection time t_3. After those response functions have been evaluated, various components of the 2DES spectra, such as the ground state bleach (GSB) contribution $S_{\mathrm{GSB}}(\omega_\tau, T_w, \omega_t)$ and the stimulated emission (SE) contribution $S_{\mathrm{SE}}(\omega_\tau, T_w, \omega_t)$, can be expressed in terms of doubly performed Fourier transforms of the corresponding third-order response functions. Here, ω_τ and ω_t are the frequency domain equivalents of coherence time t_1 and detection t_3, respectively.

More details of the derivation of the third-order response functions and the evaluation of 2DES signals can be found in Appendix B.

III. NUMERICAL RESULTS

A. Model parameters

In this work, we systematically consider two models of the primary SF Hamiltonian H_S. The first one, the two-mode model, is essentially the model suggested in Ref. 7 and further exploited in Ref. 9. This model contains a low-frequency coupling mode Q_c and a single high-frequency tuning mode Q_{t1}. The second model, the three-mode model, contains an extra low-frequency tuning mode Q_{t2}. Our motivation behind the consideration of the three-mode model is twofold. First, there are indications that extra low-frequency tuning modes may be necessary for a detailed modeling of the SF process in rubrene. Second, an additional low-frequency tuning mode increases the sensitivity of the model to temperature effects that are in focus of the present study. Numerical values of the model parameters are collected in Table I.

The phonon bath of Eqs. (7) and (8) is fully characterized by its spectral density $D(\omega) = \sum_q \kappa_q^2 \delta(\omega - \Omega_q)$. In our simulations, the spectral density function is taken in the Drude form

$$D(\omega) = 2\eta \frac{\gamma\omega}{\omega^2 + \gamma^2}, \tag{18}$$

where $\eta = 0.15$ eV and $\gamma = 0.03$ eV. With these parameters, the bath covers the typical values of electronic dephasing times (~10 fs–100 fs) and describes their decrease with temperature. Following Ref. 7, we assume that the state S_1 is optically bright from the ground state, while the state TT is optically dark. Hence, we set $\mu_{gS1} = 1$ and $\mu_{gTT} = 0$.

Shown in Figs. 1 and 2 are the cuts through adiabatic PESs of the electronic ground state g (black) and two excited S_1 (blue)

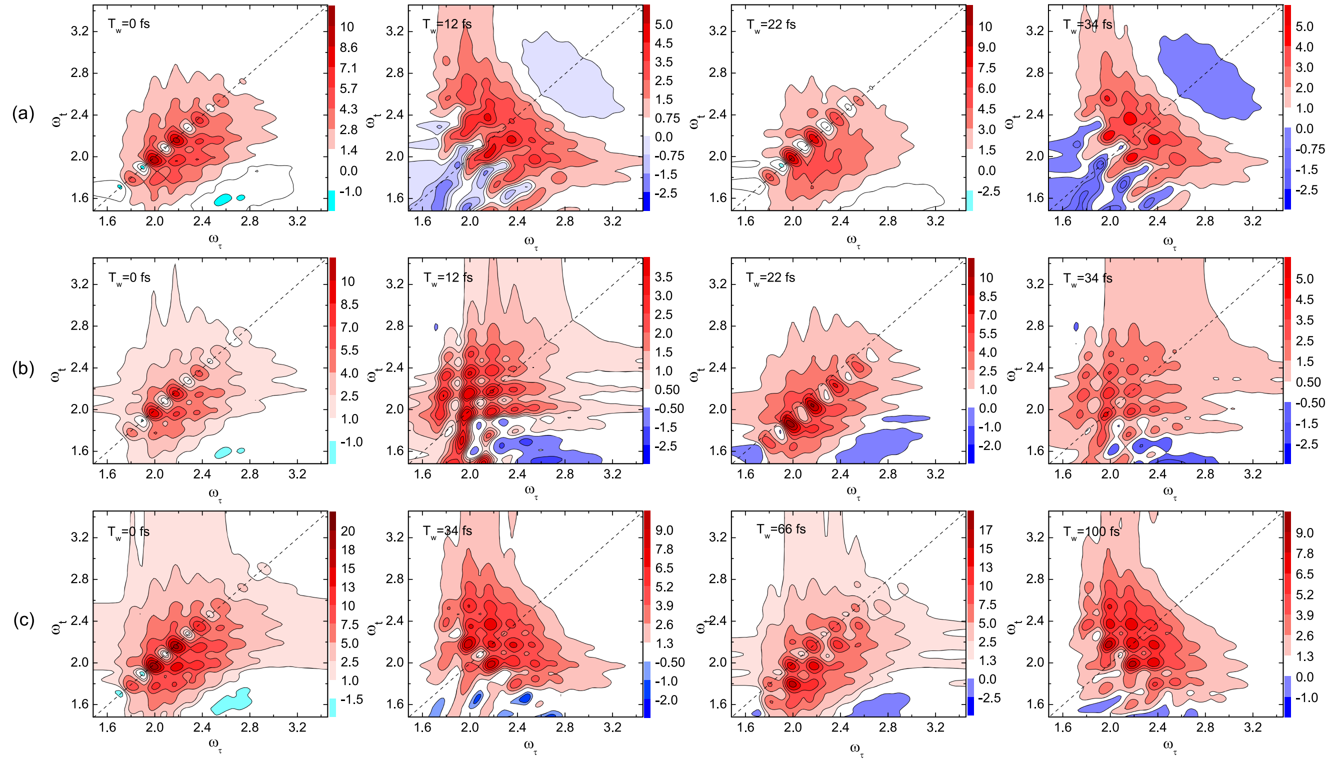

FIG. 4. The real parts of the SE component (a), the GSB component (b), and the total 2DES signals (c) in the two-mode model for different population times T_w at T = 10 K. [(a) and (b)] From left to right, the spectra correspond to T_w = 0 fs, 12 fs, 22 fs, and 34 fs. (c) From left to right, the spectra correspond to T_w = 0 fs, 34 fs, 66 fs, and 100 fs.

and S_{TT} (red) electronic states of the 2-mode model and the 3-mode model along the corresponding normal coordinates, respectively. The CI is located at $(Q_c, Q_{t1}) = (0, 0.07)$ for the 2-mode model and at $(Q_c, Q_{t1}, Q_{t2}) = (0, 0.07, 0.325)$ for the 3-mode model. In both models, the CIs are, therefore, located in the vicinity of the Franck–Condon region $(Q_c, Q_{t1}, Q_{t2}) = (0, 0, 0)$. The vertical energy corresponding to the CI is found to be 2.256 eV in both models.

B. Temperature effects on population dynamics

We first investigate the temperature effect on the population dynamics $P(t)$ of the S_1 state in the two-mode $(\Omega_{c,t1})$ and the three-mode $(\Omega_{c,t1,t2})$ CI model of the SF process. The thermal bath of Eqs. (7) and (8) does not affect $P(t)$. Hence, $P(t)$ exhibits the net effect of the temperature-dependent dynamics driven by the system Hamiltonian H_S alone.

The population dynamics of $P(t)$ for both models is presented in Fig. 3 for a range of temperatures from 0 K to 300 K. The population decay (hence, the SF efficiency) increases with temperature in both models. This can be understood by the following considerations. Using the explicit form of H_S, it is straightforward to show that the initial depopulation dynamics is Gaussian,

$$\langle P(t)\rangle = \exp\{-\nu^2 t^2\} + O(t^3),$$

where ν^{-1} is the so-called Zeno time that can be evaluated according to Refs. 47 and 48. Explicitly,

$$\nu^2 = \lambda^2\langle Q_c^2\rangle = \lambda^2\left(\frac{1}{2} + \frac{1}{\exp\{\Omega_c/(k_B T)\} - 1}\right). \tag{19}$$

Hence, the population decay rate ν is minimal at $T = 0$ ($\nu = \lambda/\sqrt{2}$) and increases ~ $\sqrt{T}$ in the classical limit of $k_B T \gg \Omega_c$, yielding $\nu = \lambda\sqrt{k_B T/\Omega_c}$. The initial decay of $P(t)$ is, thus, determined solely by the frequency of the coupling mode Ω_c and temperature T and is independent of the tuning modes, in agreement with the temperature dependency of initial population dynamics in Fig. 3.

At $t > \nu^{-1}$, the $P(t)$ evolution becomes much more complex and depends strongly on the tuning modes. In particular, the depopulation in the 3-mode model is faster than that in the 2-model model. This indicates that thermally activated modes accelerate the SF process. For $t < 75$ fs [Fig. 3(a)] and $t < 200$ fs [Fig. 3(b)], $P(t)$ exhibits a characteristic step-like structure that is characterized by the period of $2\pi/\Omega_{t1} = 22$ fs, revealing the high-frequency tuning mode. This structure is indicative of the stepwise, CI-driven $|S_1\rangle \to |TT\rangle$ population transfer. This kind of behavior is generic for nonadiabatic vibronic systems (see Ref. 49 and the discussion therein). On a longer timescale, $P(t)$ of Fig. 3(a) exhibits a

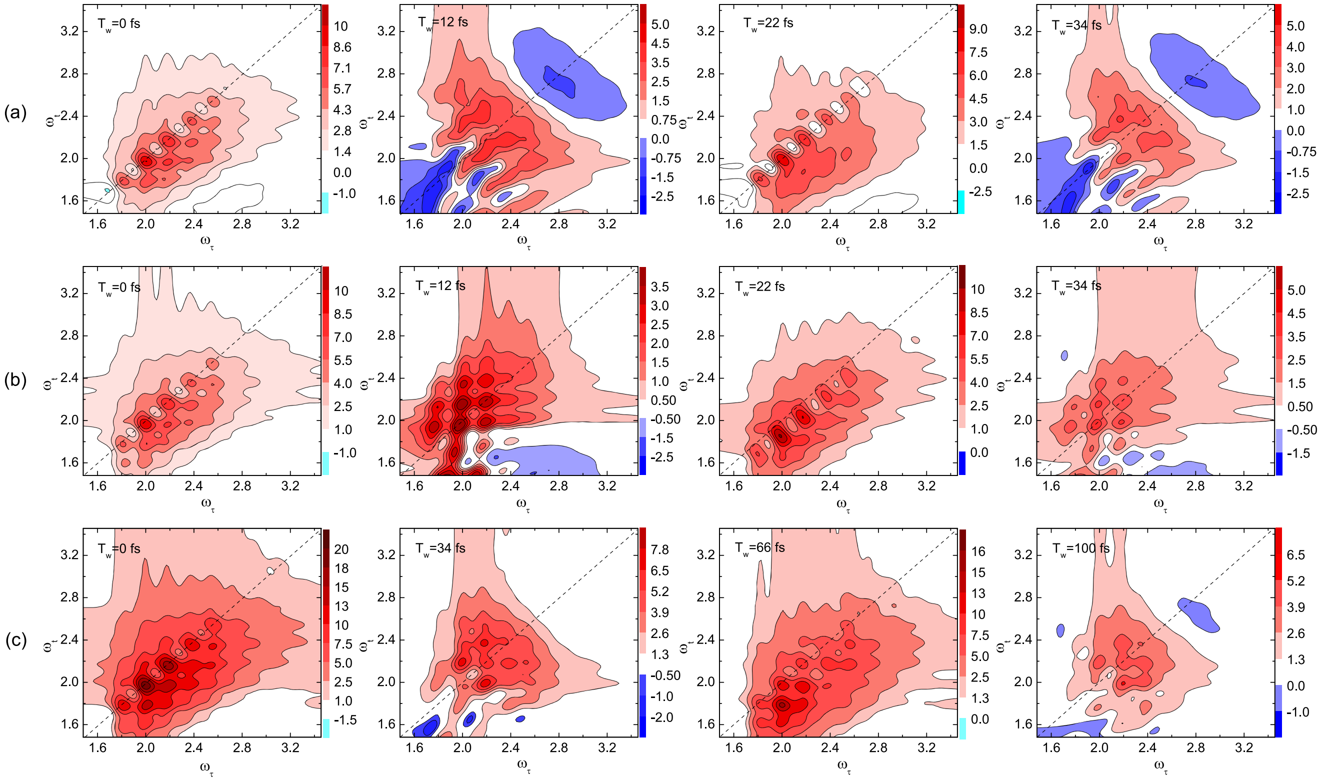

FIG. 5. The real parts of the SE component (a), the GSB component (b), and the total 2DES signals (c) in the two-mode model for different population times T_w at T = 100 K. [(a) and (b)] From left to right, the spectra correspond to T_w = 0 fs, 12 fs, 22 fs, and 34 fs. (c) From left to right, the spectra correspond to T_w = 0 fs, 34 fs, 66 fs, and 100 fs.

quite erratic behavior, which is typical for two-mode CIs.[14] The dynamics of $P(t)$ in Fig. 3(b) is smoother, faster, and more irreversible since more modes are involved in the CI-driven population transfer.

C. Temperature effects in 2D spectra

We begin with a systematic investigation of 2DES spectra for the two-mode model at various waiting times T_w and three temperatures [T = 10 K (Fig. 4), T = 100 K (Fig. 5), and T = 300 K (Fig. 6)]. Any 2DES signal can be subdivided into three components: the GSB component, the SE component, and the excited state absorption (ESA) component. The GSB contribution reflects the wave packet motion in the electronic ground state, while two other contributions monitor the projection of the wave packet motion in the low-lying electronic states into the electronic ground state (GSB) and the higher-lying electronic states (ESA). Since the higher-lying electronic states are not included in our model, ESA is not considered here. We, thus, plot separately the SE contribution (a), the GSB contributions (b), and the total (SE + GSB) 2DES spectra (c).

It should be recapitalized here that the thermal bath of Eqs. (7) and (8) is responsible for optical dephasing only, with the dephasing rates increasing with temperature. The bath broadens the peaks in the 2D spectra but does not affect dynamical features in the signals. The latter are determined by the system dynamics driven by the Hamiltonian H_S at different temperatures.

Let us consider Fig. 4 first. Since T = 10 K causes weak dephasing in the present model, the spectra show pronounced peaks of vibronic progression, which reveal the high-frequency tuning mode Ω_{t1}. At T_w = 0, the SE, GSB, and total signal look similar and are concentrated along the main diagonal. The strongest diagonal peaks are located at two points, (ω_τ, ω_t) = (2.0 eV, 2.0 eV) and (2.18 eV, 2.18 eV): The first of which matches the 0–0 vertical excitation energy of the system, also known as the zero-phonon line. The other point, (2.18 eV, 2.18 eV), is the 0–1 peak in a corresponding vibronic progression of linear absorption. At T_w = 12 fs, which corresponds to the half-period of the high-frequency tuning mode, shapes of the SE and GSB contributions change. The SE signal remains symmetric with respect to the main diagonal but spreads over both directions (ω_τ and ω_t). This reflects the pulsating character of the wave packet propagation. The GSB signal also spreads along both axes (ω_τ and ω_t) but loses its axial symmetry, developing a pattern shifted predominantly above the main diagonal ($\omega_t > \omega_\tau$) but possessing a substantial below diagonal lobe. This behavior reflects the reversible energy redistribution in the electronic ground state, which populates those vibrational levels that have larger Franck–Condon factors with higher lying vibronic levels in the excited electronic states. T_w = 24 fs corresponds to the period of the Ω_{t1} mode. We, thus, observe an almost complete revival of the GSB, SE, and total signal because the $|S_1\rangle \to |TT\rangle$ population transfer at t = 24 fs is just around 4% (cf. Fig. 3). As T_w increases, the SE and GSB

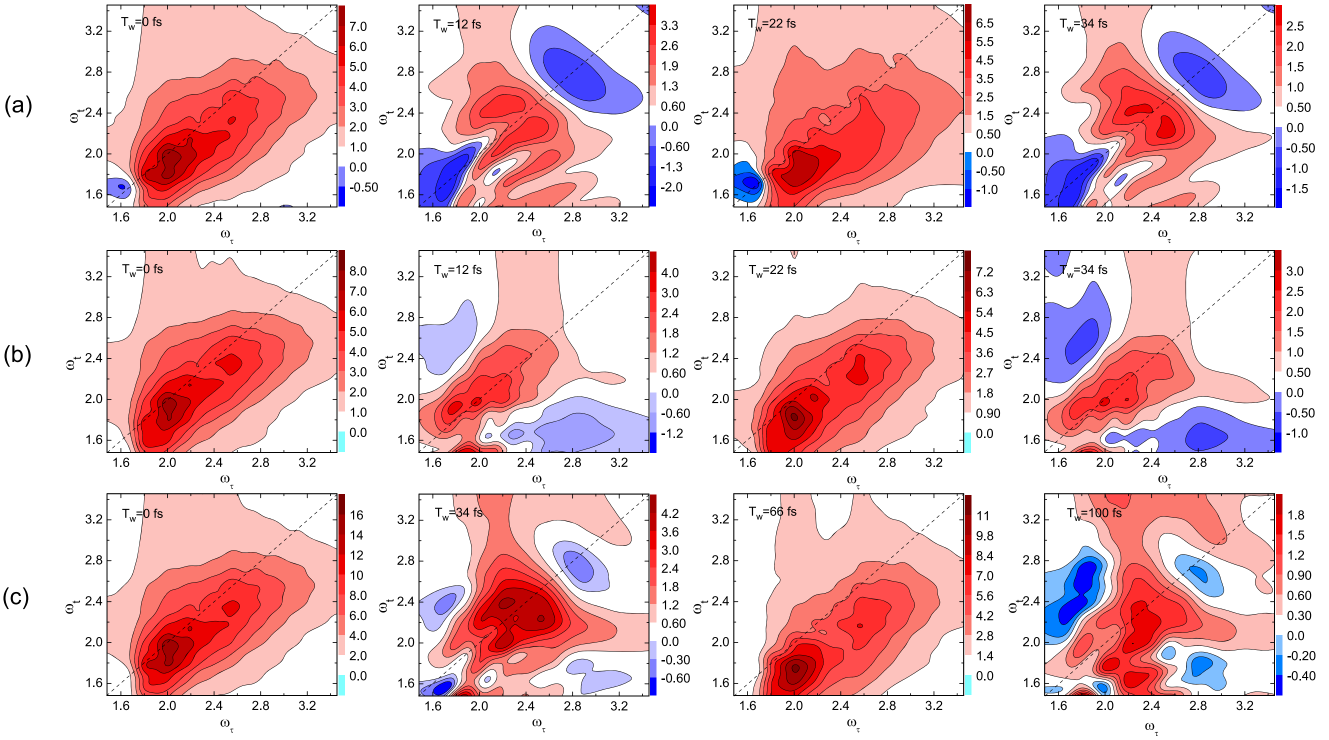

FIG. 6. The real parts of the SE component (a), the GSB component (b), and the total 2DES signals (c) in the two-mode model for different population times T_w at T = 300 K. [(a) and (b)] From left to right, the spectra correspond to T_w = 0 fs, 12 fs, 22 fs, and 34 fs. (c) From left to right, the spectra correspond to T_w = 0 fs, 34 fs, 66 fs, and 100 fs.

signals exhibit almost periodic evolution with a period of 22 fs. Yet, negative areas along the main diagonal are formed in the SE signals and below the main diagonal in the GSB signals. This can be related to the rephasing of the wave packet motion in the electronic ground and the excited states (cf. Refs. 35 and 50). In general, intensities of the SE and GSB signals are comparable on the entire timescale under consideration (~100 fs), and both the SE and GSB components contribute almost equally to the total 2DES signal, the intensity of which decreases only slightly with T_w. This is a manifestation of the relatively slow $|S_1\rangle \rightarrow |\mathrm{TT}\rangle$ population transfer (cf. Fig. 3).

The 2DES spectra at T = 100 K are plotted in Fig. 5. The 2DES spectra are similar to those at T = 10 K. However, the rising temperature causes two different effects. On the one hand, it increases the number of system states amenable to spectroscopic probing. On the other hand, it causes stronger bath-induced electronic dephasing. The first effect is not significant since $\Omega_c/(k_B T)$ = 1.8 at T = 100 K. It induces a faster $|S_1\rangle \rightarrow |\mathrm{TT}\rangle$ population transfer, which manifests itself in slightly smaller SE intensities. The second effect broadens vibrational peaks.

If the temperature further increases, the effects described above become more dramatic. The corresponding 2DES signals at T = 300 K are shown in Fig. 6. Since $\Omega_c/(k_B T)$ = 0.6 at T = 300 K, temperature effects cause significant dynamical changes, which manifest themselves through the pronounced asymmetry of the signals relative to the main diagonal. In addition, the aforementioned 22 fs periodicity of the signals is complied with only approximately since more states connected to the coupling mode are involved in the CI-driven dynamics. On the other hand, a substantial increase of the optical dephasing merges individual vibrational peaks into richly structured, multiform patterns that are the two-dimensional manifestations of the linear vibronic progression.

Let us consider now 2DES signals for the three-mode model. The signals simulated at T = 100 K are depicted in Fig. 7. Albeit the general patterns and trends of the two-mode model in Fig. 5 have been reproduced in Fig. 7, the difference between the two is still quite dramatic. First, the 2DES signals in Fig. 7 lose almost completely the vibronic structure of Fig. 5. Second, the shapes of the signals undergo significant changes, most notably at larger values of T_w. This is a direct consequence of the increased density of states in the three-mode model of SF.

The 2DES signals simulated at T = 300 K in the three-mode model, as shown in Fig. 8, should be contrasted with their two-mode model counterparts in Fig. 6. The differences between the two groups of signals are even more substantial. The signals of the three-mode model show less-structured patterns with more pronounced asymmetry relative to the main diagonal, as compared with those of the two-model model. Hence, we conclude that vibronic effects triggered by low-frequency modes become more pronounced at elevated temperatures.

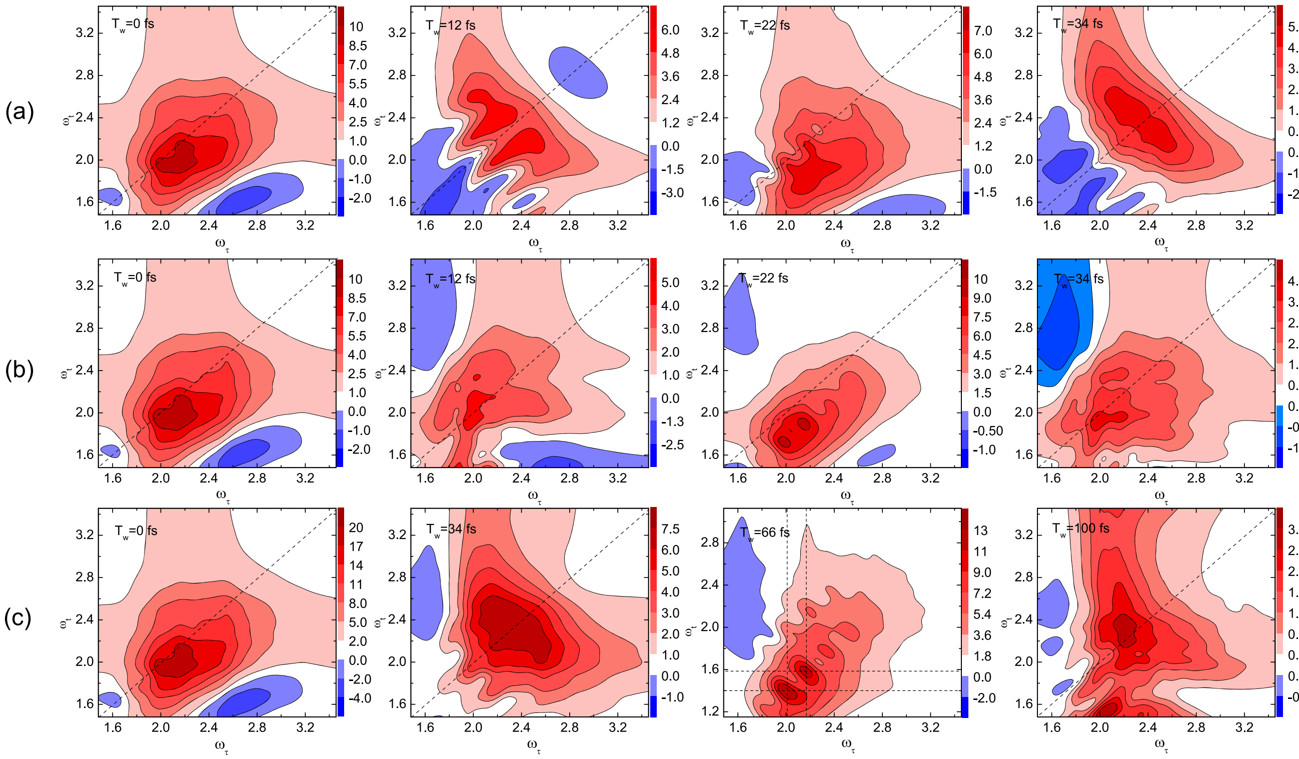

FIG. 7. The real parts of the SE component (a), the GSB component (b), and the total 2DES signals (c) in the three-mode model for different population times T_w at T = 100 K. [(a) and (b)] From left to right, the spectra correspond to T_w = 0 fs, 12 fs, 22 fs, and 34 fs. (c) From left to right, the spectra correspond to T_w = 0 fs, 34 fs, 66 fs, and 100 fs.

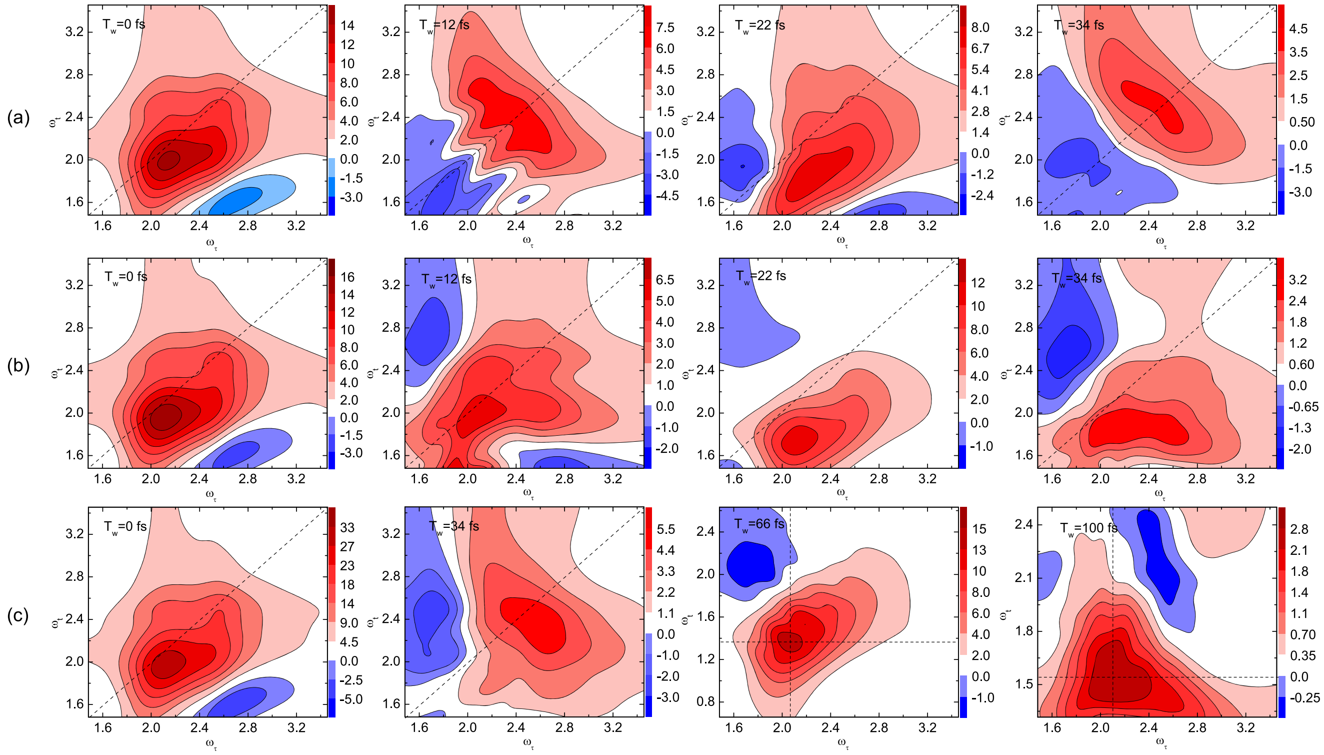

FIG. 8. The real parts of the SE component (a), the GSB component (b), and the total 2DES signals (c) in the three-mode model for different population times T_w at T = 300 K. [(a) and (b)] From left to right, the spectra correspond to T_w = 0 fs, 12 fs, 22 fs, and 34 fs. (c) From left to right, the spectra correspond to T_w = 0 fs, 34 fs, 66 fs, and 100 fs.

IV. CONCLUSIONS

To develop a microscopic methodology for the accurate simulation of multidimensional spectroscopic signals of SF systems, we have extended the variational Davydov *Ansatz* machinery toward the evaluation of third-order response functions at finite temperatures. This allows us to simulate 2DES signals of two-mode and three-mode models of crystalline rubrene in the temperature ranges relevant for many practical applications (from 0 K to 300 K). On the one hand, our simulations demonstrate that an elevated temperature facilitates the $|S_1\rangle \rightarrow |TT\rangle$ population transfer and, thus, accelerates the SF process. On the other hand, increasing temperature causes dramatic changes in 2DES spectra owing to temperature-dependent electronic dephasing and an increased number of system eigenstates amenable to spectroscopic probing. We, thus, conclude that thermal effects on singlet fission dynamics have to be adequately accounted for in theoretical simulations of excited state transfer and relaxation in organic molecular aggregates.

Our results demonstrate that the methodology developed in the present work to efficiently compute finite-temperature SF dynamics and associated third-order response functions and 2DES signals can be readily applied to novel material systems with one or a few vibrational modes exhibiting strong intrastate vibrational coupling and/or strong interstate electronic coupling. Furthermore, in the anticipation of rapid progress in spectroscopic technologies and the need to probe ultrafast excitation transfer of multiple segments, higher-order optical response functions and multidimensional spectroscopic signals beyond third-order can be computed using the same methodology established here. The work along this direction as well as the extension of the present framework to account for higher-lying electronic states is in progress.

ACKNOWLEDGMENTS

The authors thank Frank Grossmann for enlightening discussions. The authors gratefully acknowledge the support of the Singapore Ministry of Education Academic Research Fund Tier 1 (Grant No. RG190/18) and Tier 2 (Grant No. MOE2019-T2-1-085). M. F. Gelin acknowledges the support of Hangzhou Dianzi University through the startup funding. K. Sun would like to thank the Natural Science Foundation of Zhejiang Province (Grant No. LY18A040005) for support. Q. Xu acknowledges the support of the Graduate Scientific Research Foundation of Hangzhou Dianzi University.

APPENDIX A: TIME-DEPENDENT VARIATIONAL APPROACH BY THE MULTI-D$_2$ *ANSÄTZE*

1. Equation of motion

The equations that govern the time propagation of the variational parameters μ_i can be obtained from the Euler equations of motion,

$$\frac{d}{dt}\frac{\partial L}{\partial \dot{\mu}_i^*} - \frac{\partial L}{\partial \mu_i^*} = 0, \tag{A1}$$

$$\begin{aligned} L = \frac{i}{2}\left[\langle D_2^M(t)|\frac{\overrightarrow{\partial}}{\partial t}|D_2^M(t)\rangle - \langle D_2^M(t)|\frac{\overleftarrow{\partial}}{\partial t}|D_2^M(t)\rangle\right] \\ - \langle D_2^M(t)|H|D_2^M(t)\rangle =: L_{td} - L_H. \end{aligned} \tag{A2}$$

Using the normalization of the Davydov *Ansatz*, the derivative can only be taken to the right, simplifying matters considerably,

$$L_{td} = i\langle D_2^M(t)|\frac{\overrightarrow{\partial}}{\partial t}|D_2^M(t)\rangle. \tag{A3}$$

We first calculate the Lagrangian L in the Dirac–Frenkel time-dependent variation,

$$\begin{aligned} L = {} & i\sum_{m,n}^{M}\left[A_m^*\dot{A}_n + B_m^*\dot{B}_n\right]S_{mn} \\ & + i\sum_{m,n}^{M}\left[\left(A_m^*A_n + B_m^*B_n\right)\sum_q\left(\frac{\left(2f_{mq}^*\dot{f}_{nq} - f_{nq}^*\dot{f}_{nq} - f_{nq}\dot{f}_{nq}^*\right)}{2}\right)\right]S_{mn} \\ & - \langle D_2^M(t)|H|D_2^M(t)\rangle, \end{aligned} \tag{A4}$$

where the Debye–Waller factor is $S_{mn} = \exp\sum_q\left\{-\left(|f_{mq}|^2 + |f_{nq}|^2\right)/2 + f_{mq}^*f_{nq}\right\}$ and the last term in Eq. (A4) can be obtained as

$$\begin{aligned} & \left\langle D_2^M(t)\middle|H\middle|D_2^M(t)\right\rangle \\ & = \sum_{n,m}^{M}\left(\epsilon_{S_1}A_m^*A_n + \epsilon_{TT}B_m^*B_n\right)S_{mn} \\ & \quad + \sum_{n,m}^{M}\left(A_m^*A_n + B_m^*B_n\right)\sum_q\omega_q f_{mq}^*f_{nq}S_{mn} \\ & \quad + \sum_{n,m}^{M}\sum_q\left(\frac{\kappa_q^{(1)}}{\sqrt{2}}A_m^*A_n + \frac{\kappa_q^{(2)}}{\sqrt{2}}B_m^*B_n\right)\left(f_{nq} + f_{mq}^*\right)S_{mn} \\ & \quad + \sum_{n,m}^{M}\sum_q\frac{\lambda_q}{\sqrt{2}}\left(A_m^*B_n + B_m^*A_n\right)\left(f_{nq} + f_{mq}^*\right)S_{mn}. \end{aligned} \tag{A5}$$

The Dirac–Frenkel variational principle results in equations of motion for A_n and B_n,

$$\begin{aligned} & i\sum_n^M\dot{A}_nS_{mn} + i\sum_n^M A_n\sum_q\left[-\frac{1}{2}\left(\dot{f}_{nq}f_{nq}^* + f_{nq}\dot{f}_{nq}^*\right) + f_{mq}^*\dot{f}_{nq}\right]S_{mn} \\ & = \epsilon_{S_1}\sum_n^M A_nS_{mn} + \sum_n^M A_n\sum_q\omega_q f_{mq}^*f_{nq}S_{mn} \\ & \quad + \sum_n^M A_n\sum_q\frac{\kappa_q^{(1)}}{\sqrt{2}}\left(f_{nq} + f_{mq}^*\right)S_{mn} \\ & \quad + \sum_n^M B_n\sum_q\frac{\lambda_q}{\sqrt{2}}\left(f_{nq} + f_{mq}^*\right)S_{mn} \end{aligned} \tag{A6}$$

and

$$\begin{aligned} & i\sum_n^M\dot{B}_nS_{mn} + i\sum_n^M B_n\sum_q\left[-\frac{1}{2}\left(\dot{f}_{nq}f_{nq}^* + f_{nq}\dot{f}_{nq}^*\right) + f_{mq}^*\dot{f}_{nq}\right]S_{mn} \\ & = \epsilon_{TT}\sum_n^M B_nS_{mn} + \sum_n^M B_n\sum_q\omega_q f_{mq}^*f_{nq}S_{mn} \\ & \quad + \sum_n^M B_n\sum_q\frac{\kappa_q^{(2)}}{\sqrt{2}}\left(f_{nq} + f_{mq}^*\right)S_{mn} \\ & \quad + \sum_n^M A_n\sum_q\frac{\lambda_q}{\sqrt{2}}\left(f_{nq} + f_{mq}^*\right)S_{mn}. \end{aligned} \tag{A7}$$

The equations of motion for f_{nk} are

$$\begin{aligned} & i\sum_n^M\left(A_m^*\dot{A}_n + B_m^*\dot{B}_n\right)f_{nk}S_{mn} + i\sum_n^M\left(A_m^*A_n + B_m^*B_n\right)\dot{f}_{nk}S_{mn} \\ & \quad + i\sum_n^M\left(A_m^*A_n + B_m^*B_n\right)f_{nq}S_{mn}\sum_q\left[f_{mq}^*\dot{f}_{nq} - \frac{1}{2}\left(\dot{f}_{nq}f_{nq}^* + f_{nq}\dot{f}_{nq}^*\right)\right] \\ & = \sum_n^M\left(\epsilon_{S_1}A_m^*A_n + \epsilon_{TT}B_m^*B_n\right)f_{nk}S_{mn} + \sum_n^M\left(A_m^*A_n + B_m^*B_n\right)\omega_k f_{nk}S_{mn} \\ & \quad + \sum_n^M f_{nk}\sum_q\left(A_m^*A_n + B_m^*B_n\right)\omega_q f_{mq}^*f_{nq}S_{mn} \\ & \quad + \sum_n^M\left(A_m^*A_n\frac{\kappa_k^{(1)}}{\sqrt{2}} + B_m^*B_n\frac{\kappa_k^{(2)}}{\sqrt{2}}\right)S_{mn} \\ & \quad + \sum_n^M f_{nk}\sum_q\left(A_m^*A_n\frac{\kappa_q^{(1)}}{\sqrt{2}} + B_m^*B_n\frac{\kappa_q^{(2)}}{\sqrt{2}}\right)\left(f_{nq} + f_{mq}^*\right)S_{mn} \\ & \quad + \sum_n^M\left(A_m^*B_n\frac{\lambda_k}{\sqrt{2}} + B_m^*A_n\frac{\lambda_k}{\sqrt{2}}\right)S_{mn} \\ & \quad + \sum_n^M f_{nk}\sum_q\left(A_m^*B_n\frac{\lambda_q}{\sqrt{2}} + B_m^*A_n\frac{\lambda_q}{\sqrt{2}}\right)\left(f_{nq} + f_{mq}^*\right)S_{mn}. \end{aligned} \tag{A8}$$

APPENDIX B: 2D SPECTRA

All optical response functions hinge on the transition dipole moment; the auto-correlation functions of the polarization operator directly lead to linear and nonlinear spectral signals. The autocorrelation function $F(t)$ based on the multi-D_2 *Ansätze* is defined by

$$\begin{aligned} F(t) & = {}_{\text{ph}}\langle 0|_{ex}\langle 0|e^{iHt}Pe^{-iHt}|0\rangle_{\text{ex}}|0\rangle_{\text{ph}} \\ & = {}_{\text{ph}}\langle 0|_{ex}\langle 0|Pe^{-iHt}P^{\dagger}|0\rangle_{\text{ex}}|0\rangle_{\text{ph}}, \end{aligned} \tag{B1}$$

where $P = \mu\sum_n(|n\rangle_{\text{exex}}\langle 0| + |0\rangle_{\text{exex}}\langle n|)$ is the polarization operator.

The linear absorption spectra are ready to be obtained by the Fourier transformation of the autocorrelation function,[51] which reads

$$F(\omega) = \frac{1}{\pi} Re \int_0^\infty F(t)dt. \tag{B2}$$

In addition to the information provided by the linear (1D) spectra, 2DES signals provide direct knowledge on multi-state excitonic dynamics and inter-exciton interactions and on dephasing and relaxation processes that are elusive in the output from the traditional 1D spectroscopy. The computation of 2DES signals involves calculating the third-order polarization $P^{(3)}(t)$, which can be expressed in terms of the nonlinear response function $R_i(\tau, T_w, t)$ with i going from 1 to 4, and τ and t are the coherence time and the detection time, respectively.

In the SF model of Sec. II A, the total response functions can be represented as the product of the responses generated by the system and bath Hamiltonians,

$$R_i(\tau, T_w, t) = R_i^S(\tau, T_w, t) R_i^B(\tau, T_w, t). \tag{B3}$$

The reader is referred to Ref. 9 for a detailed derivation and explicit expressions for $R_i^S(\tau, T_w, t)$ in terms of the multi-D_2 *Ansätze*. $R_i^B(\tau, T_w, t)$, on the other hand, are evaluated analytically,[52]

$$\begin{aligned}
R_1^B(\tau, T_w, t) &= e^{-g^*(t)-g(\tau)-g^*(T_w)+g^*(T_w+t)+g(\tau+T_w)-g(\tau+T_w+t)},\\
R_2^B(\tau, T, t) &= e^{-g^*(t)-g^*(\tau)+g(T_w)-g(T_w+t)-g^*(\tau+T_w)+g^*(\tau+T_w+t)},\\
R_3^B(\tau, T_w, t) &= e^{-g(t)-g^*(\tau)+g^*(T_w)-g^*(T_w+t)-g^*(\tau+T_w)+g^*(\tau+T_w+t)},\\
R_4^B(\tau, T_w, t) &= e^{-g(t)-g(\tau)-g(T_w)+g(T_w+t)+g(\tau+T_w)-g(\tau+T_w+t)},
\end{aligned} \tag{B4}$$

where $g(t)$ is the line shape function,

$$\begin{aligned}
g(t) = &\int_0^\infty d\omega \frac{D(\omega)}{\omega^2}\\
&\times \left[\coth \frac{\hbar\omega}{2k_B T_{eq}} (1 - \cos \omega t) + i(\sin \omega t - \omega t)\right].
\end{aligned} \tag{B5}$$

If the laser pulses are short on the timescale of the system dynamics, the SE and GSB contributions to the 2DES signals are directly expressed through the response functions as follows:

$$\begin{aligned}
S_{\text{SE}}(\omega_\tau, T_w, \omega_t) = \Re &\int_0^\infty \int_0^\infty dt d\tau \Big[R_2(\tau, T_w, t) e^{-i\omega_\tau \tau + i\omega_t t}\\
&+ R_4(\tau, T_w, t) e^{i\omega_\tau \tau + i\omega_t t} \Big],\\
S_{\text{GSB}}(\omega_\tau, T_w, \omega_t) = \Re &\int_0^\infty \int_0^\infty dt d\tau \Big[R_3(\tau, T_w, t) e^{-i\omega_\tau \tau + i\omega_t t}\\
&+ R_1(\tau, T_w, t) e^{i\omega_\tau \tau + i\omega_t t} \Big].
\end{aligned} \tag{B6}$$

The correlated 2D spectrum (ω_τ, T_w, ω_t) is given by the sum of the two above contributions, neglecting the contribution of ESA (excited-state absorption),

$$S(\omega_\tau, T_w, \omega_t) = S_{SE}(\omega_\tau, T_w, \omega_t) + S_{GSB}(\omega_\tau, T_w, \omega_t). \tag{B7}$$

DATA AVAILABILITY

The data that support the findings of this study are available from the corresponding author upon reasonable request.

REFERENCES

[1] M. B. Smith and J. Michl, Chem. Rev. **110**, 6891 (2010).

[2] A. Japahuge and T. Zeng, ChemPlusChem **83**, 146 (2018).

[3] S. Ito, T. Nagami, and M. Nakano, J. Photochem. Photobiol., C **34**, 85 (2018).

[4] D. Casanova, Chem. Rev. **118**, 7164 (2018).

[5] K. Miyata, F. S. Conrad-Burton, F. L. Geyer, and X.-Y. Zhu, Chem. Rev. **119**, 4261 (2019).

[6] A. J. Musser, M. Liebel, C. Schnedermann, T. Wende, T. B. Kehoe, A. Rao, and P. Kukura, Nat. Phys. **11**, 352 (2015).

[7] K. Miyata, Y. Kurashige, K. Watanabe, T. Sugimoto, S. Takahashi, S. Tanaka, J. Takeya, T. Yanai, and Y. Matsumoto, Nat. Chem. **9**, 983 (2017).

[8] H.-G. Duan, A. Jha, X. Li, V. Tiwari, H. Ye, P. K. Nayak, X.-L. Zhu, Z. Li, T. J. Martinez, M. Thorwart, and R. J. D. Miller, Sci. Adv. **6**, eabb0052 (2020).

[9] K. W. Sun, Z. K. Huang, M. F. Gelin, L. P. Chen, and Y. Zhao, J. Chem. Phys. **151**, 114102 (2019).

[10] J. Sung, P. Kim, B. Fimmel, F. Würthner, and D. Kim, Nat. Commun. **6**, 8646 (2015).

[11] C. Kaufmann, W. Kim, A. Nowak-Król, Y. Hong, D. Kim, and F. Würthner, J. Am. Chem. Soc. **140**, 4253 (2018).

[12] A. A. Bakulin, S. E. Morgan, T. B. Kehoe, M. W. B. Wilson, A. W. Chin, D. Zigmantas, D. Egorova, and A. Rao, Nat. Chem. **8**, 16 (2016).

[13] Y. Tanimura, J. Chem. Phys. **153**, 020901 (2020).

[14] L. P. Chen, M. F. Gelin, V. Y. Chernyak, W. Domcke, and Y. Zhao, Faraday Discuss. **194**, 61 (2016).

[15] L. P. Chen, Y. Zhao, and Y. Tanimura, J. Phys. Chem. Lett. **6**, 3110 (2015).

[16] A. G. Dijkstra and V. I. Prokhorenko, J. Chem. Phys. **147**, 064102 (2017).

[17] T. Ikeda and Y. Tanimura, Chem. Phys. **515**, 203 (2018).

[18] D.-L. Qi, H.-G. Duan, Z.-R. Sun, R. J. D. Miller, and M. Thorwart, J. Chem. Phys. **147**, 074101 (2017).

[19] H.-G. Duan, D.-L. Qi, Z.-R. Sun, R. J. D. Miller, and M. Thorwart, Chem. Phys. **515**, 21 (2018).

[20] H.-G. Duan, R. J. D. Miller, and M. Thorwart, J. Phys. Chem. Lett. **7**, 3491 (2016).

[21] M. Sala and D. Egorova, Chem. Phys. **481**, 206–217 (2016).

[22] L. P. Chen, M. F. Gelin, Y. Zhao, and W. Domcke, J. Phys. Chem. Lett. **10**, 5873 (2019).

[23] W. Domcke and G. Stock, Adv. Chem. Phys. **100**, 1 (1997).

[24] H. D. Meyer, F. Gatti, and G. A. Worth, *Multidimensional Quantum Dynamics: MCTDH Theory and Applications* (Wiley-VCH, Weinheim, 2009).

[25] G. W. Richings, I. Polyak, K. E. Spinlove, G. A. Worth, I. Burghardt, and B. Lasorne, Int. Rev. Phys. Chem. **34**, 269 (2015).

[26] H. Wang, X. Song, D. Chandler, and W. H. Miller, J. Chem. Phys. **110**, 4828 (1999).

[27] H. Wang and M. Thoss, J. Phys. Chem. A **107**, 2126 (2003).

[28] I. Kondov, M. Thoss, and H. Wang, J. Phys. Chem. A **110**, 1364 (2006).

[29] R. Borrelli, M. Di Donato, and A. Peluso, J. Chem. Theory Comput. **3**, 673 (2007).

[30] R. Borrelli, M. Di Donato, and A. Peluso, Theor. Chem. Acc. **117**, 957 (2007).

[31] H. Wang and M. Thoss, Chem. Phys. **347**, 139–151 (2008).

[32] B. Brüggemann, P. Persson, H.-D. Meyer, and V. May, Chem. Phys. **347**, 152–165 (2008).

[33] T. D. Huynh, K.-W. Sun, M. Gelin, and Y. Zhao, J. Chem. Phys. **139**, 104103 (2013).

[34] K.-W. Sun, M. F. Gelin, V. Y. Chernyak, and Y. Zhao, J. Chem. Phys. **142**, 212448 (2015).

[35] K.-W. Sun and Y. Yao, J. Chem. Phys. **147**, 224905 (2017).

[36] L. P. Chen, M. F. Gelin, and W. Domcke, J. Chem. Phys. **150**, 024101 (2019).

[37] M. Werther, F. Grossmann, Z. K. Huang, and Y. Zhao, J. Chem. Phys. **150**, 234109 (2019).

[38] M. Werther, S. L. Choudhury, and F. Grossmann, Int. Rev. Phys. Chem. **40**, 81 (2021).

[39] L. Wang, Y. Fujihashi, L. Chen, and Y. Zhao, J. Chem. Phys. **146**, 124127 (2017).

[40] L. Chen and Y. Zhao, J. Chem. Phys. **147**, 214102 (2017).

[41] L. Chen, R. Borrelli, and Y. Zhao, J. Phys. Chem. A **121**, 8757 (2017).

[42] M. F. Gelin and R. Borrelli, Ann. Phys. **529**, 1700200 (2017).

[43] P. Domokos, P. Adam, and J. Janszky, Phys. Rev. A **50**, 4293 (1994).

[44] M. Cho, *Two-Dimensional Optical Spectroscopy* (CRC Press, Boca Raton, 2009).

[45] L. Valkunas, D. Abramavicius, and T. Mancal, *Molecular Excitation Dynamics and Relaxation* (Wiley-VCH, Weinheim, 2013).

[46] P. Hamm and M. Zanni, *Concepts and Methods of 2D Infrared Spectroscopy* (Cambridge University Press, Cambridge, 2011).

[47] P. Facchi and S. Pascazio, Fortschr. Phys. **49**, 941 (2001).

[48] M. F. Gelin, R. Borrelli, and W. Domcke, J. Phys. Chem. Lett. **10**, 2806 (2019).

[49] A. V. Pisliakov, M. F. Gelin, and W. Domcke, J. Phys. Chem. A **107**, 2657 (2003).

[50] J. Krčmář, M. F. Gelin, and W. Domcke, J. Chem. Phys. **143**, 074308 (2015).

[51] N. J. Zhou, L. P. Chen, Z. K. Huang, K. W. Sun, Y. Tanimura, and Y. Zhao, J. Phys. Chem. A **120**, 1562 (2016).

[52] S. Mukamel, *Principles of Nonlinear Optical Spectroscopy* (Oxford University Press, New York, 1995).